

**Collisionality and magnetic geometry effects  
on tokamak edge turbulent transport  
II. Many-blob turbulence in the two-region model**

**D. A. Russell, J. R. Myra and D. A. D'Ippolito**

*Lodestar Research Corporation,  
2400 Central Avenue,  
Boulder, Colorado 80301*

June, 2007

(submitted to Physics of Plasmas)

# **Collisionality and magnetic geometry effects on tokamak edge turbulent transport**

## **II. Many-blob turbulence in the two-region model**

D. A. Russell, J. R. Myra and D. A. D'Ippolito

*Lodestar Research Corp., 2400 Central Ave. P-5, Boulder, Colorado 80301*

### **Abstract**

A two-region model, coupling the outboard midplane and the X-point region, was proposed in Paper I [J. R. Myra, D. A. Russell and D. A. D'Ippolito, *Phys. Plasmas* **13**, 112502 (2006).] to study the effects of collisionality and magnetic geometry on electrostatic turbulent transport in the edge and scrape-off layer of a diverted tokamak plasma by filamentary coherent structures or “blobs.” Attention was focused on the properties of isolated blobs. That study is extended here to the many-blob, turbulent saturated state driven by a linearly unstable density profile. The evolution of the density profile is included. It is demonstrated that turbulent density transport increases with collisionality but decreases with enhanced magnetic field-line fanning and shear in this model. Field-line shear induces poloidal velocity in isolated blob propagation and decorrelates the electrostatic potentials in the two regions in the turbulent regime. PDFs of density flux resemble those of experimental probe data: both are insensitive to magnetic field geometry and collisionality. It is shown that blobs are born where the skewness of density fluctuations vanishes and the logarithmic pressure gradient is maximized. The simulations show increased particle fluxes with increased plasma resistivity, which are due to increases in both blob velocity and creation rate (or spatial “packing fraction”). A wavelet-type Gaussian-fitting analysis is used to study the dependence of blob velocity on blob size. It is found that streamers, which dominate the simulations, move faster than circular blobs when the two regions are electrically disconnected.

## I. Introduction

This is the second in a series of papers on the effects of collisionality and magnetic geometry on edge turbulence and blob transport. In the first paper,<sup>1</sup> hereafter referred to as I, the general motivation for this study was given. Briefly, it is well-known from the linear theory of resistive ballooning modes<sup>2</sup> and resistive X-point modes<sup>3</sup> that the collisional edge and scrape-off-layer (SOL) plasma becomes more unstable as the collisionality increases and this effect is enhanced in X-point geometry. Later nonlinear turbulence simulations<sup>4-6</sup> and experimental measurements<sup>7</sup> showed that the general level of turbulent fluctuations increases with collisionality, eventually resulting in a density limit. Analysis of blob propagation in the collisional regime of a 3D simulation showed that blobs moved faster and disconnected from the divertor region (similar to the behavior of the underlying linear instability) as the collisionality increased.<sup>8</sup> However, such 3D simulations are expensive and not well-suited to extensive parameter studies. This motivated the development of a simpler numerical model, which will be referred to as the “two-region model”.

In this model, the physics parallel to  $\mathbf{B}$  is included by coupling two radial-poloidal planes, one at the outer midplane (OM) and one at the divertor or X-point (XP) region. The parallel current coupling the two 2D regions is *reduced* to the difference between the two electrostatic potentials, evaluated on the same magnetic field line, times a parallel conductivity. Flux tube fanning and shear in the X-point region enter as parameters in the linear field-line mapping between the two regions. This reduced model permits the simulation of three-dimensional effects (such as disconnection) with computational effort comparable to a 2D turbulence code.

Analysis of this model, performed in Paper I, recovered well-known linear mode structures and growth rates in different regimes of collisionality. A blob dispersion relation, obtained by applying a “blob correspondence rule”<sup>9</sup> to the linear dispersion

relation, predicted the speed-up of isolated, circular blobs with increased collisionality. This effect was observed in two-region model simulations reported in I and the quantitative agreement between analytical models and simulation results was surprisingly good. Thus, the essential blob propagation physics of the earlier 3D simulations<sup>8</sup> was recovered in the two-region model. In the present paper, these results are extended to the many-blob turbulence regime, in which the blobs are produced self-consistently by the nonlinear saturation of the turbulence. In addition to questions of blob propagation, the turbulence simulations allow us to address questions of blob creation and turbulent statistics.

The main results of this study can be summarized as follows:

- 1) Magnetic shear de-correlates the plasma potential along the field line;
- 2) Radial streamers move faster than blobs (in collisional regimes where the ion polarization current is important);
- 3) Collisionality and X-point geometry enhance blob disconnection from the divertor region;
- 4) Blob transport contributes an order unity fraction of the turbulent transport in the SOL and determines its scaling with parameters;
- 5) X-point geometry reduces the turbulent particle flux and the blob velocity;
- 6) Collisionality increases the turbulent flux and the blob velocity;
- 7) The blob birth zone is located where the linear growth rate is maximized, and this occurs where the skewness of the turbulent fluctuations vanishes,  $S = 0$ ;
- 8) The probability distribution function (PDF) of the turbulent particle flux is insensitive to the detailed physical regime (here, collisionality and geometry), as observed in experiments.

Wherever possible, we will compare these simulation results with experimental observations.

The plan of this paper is the following. In Sec. II we summarize the two-region model and in Sec. III we review its analytic properties. The simulation results are described in Sec. IV and our conclusions are given in Sec. V. Numerical details are

described in Appendices: the algorithm in Appendix A, the numerical implementation of the magnetic mapping in Appendix B, and a wavelet-like analysis in Appendix C.

## II. The Model

The two-region model equations and their elementary properties were developed in paper I.<sup>1</sup> Here we summarize that model with minor extensions that enable the present turbulence study.

The two-region model is motivated by considering the effects of magnetic field line fanning and shear on the geometry of a flux tube. In the plane normal to  $\mathbf{B}$ , with local Cartesian variables  $\mathbf{x} = (x, y)$ , where  $x$  and  $y$  are the radial and bi-normal (approximately poloidal) directions, we consider the transformation that relates displacements perpendicular to the magnetic field at different positions along a field line

$$d\mathbf{x}_2 = M \cdot d\mathbf{x}_1 \quad (1)$$

$$M = \begin{pmatrix} 1/f & 0 \\ \xi & f \end{pmatrix} \quad (2)$$

Here  $f (< 1)$  describes field-line fanning (e.g., elliptical distortion of the flux surfaces near an X-point) and  $\xi$  is a metric coefficient describing the magnetic shear (See Appendix A of Paper I.). The determinant of  $M$  is unity and so total magnetic flux inside a flux tube is conserved, i.e.  $B_1 dx_1 dy_1 = B_2 dx_2 dy_2$ , where here  $B_1 = B_2 = \text{const.}$

The basic equations of the 2D model in the plane normal to  $\mathbf{B}$  are the standard vorticity and continuity equations for two regions (each averaged along a portion of a field line), coupled by conservative charge flow (i.e. finite parallel conductivity) between the regions. To these basic equations of Paper I we add diffusion of vorticity and density and include a restorative density source in the edge region in order to sustain the turbulence against transport losses to an out-going radial boundary condition:

$$(\partial_t + \mathbf{v}_1 \cdot \nabla_1) \nabla_1^2 \Phi_1 = \sigma_{12}(\Phi_1 - \Phi_2)/n_1 - \beta \partial_{y1} \ln(n_1) + \mu_1 \nabla_1^4 \Phi_1 \quad (3)$$

$$(\partial_t + \mathbf{v}_1 \cdot \nabla_1) n_1 = D_1 \nabla_1^2 n_1 + S_1 \quad (4)$$

$$(\partial_t + \mathbf{v}_2 \cdot \nabla_2) \nabla_2^2 \Phi_2 = -\sigma_{12}(\Phi_1 - \Phi_2)/n_2 + \sigma_{23} \Phi_2 + \mu_2 \nabla_2^4 \Phi_2 \quad (5)$$

$$(\partial_t + \mathbf{v}_2 \cdot \nabla_2) n_2 = D_2 \nabla_2^2 n_2 + S_2 \quad (6)$$

where the convective  $\mathbf{E} \times \mathbf{B}$  velocity is given by

$$\mathbf{v}_j = (\mathbf{e}_z \times \nabla \Phi)_j \quad (7)$$

and, in the locally Cartesian space,  $\mathbf{e}_z = \mathbf{b} = \mathbf{B}/B$ . We assume  $T_e = \text{constant}$  and  $T_i \ll T_e$ . Here we employ the Bohm normalization: time scales normalized to  $\Omega_i = eB/m_i c$ , space scales to  $\rho_s = c_s / \Omega_i$ , where  $c_s$  is the sound speed based on the electron temperature  $T_e$ , and electrostatic potential  $\Phi$  normalized to  $T_e/e$ . These equations have been employed as the starting point for analytical work elucidating blob parameter regimes discussed in paper I and summarized in Sec. III below. Similar equations, generalized to include a temperature equation, were used to study a thermal catastrophe in the SOL plasma and a convective density limit associated with turbulent transport.<sup>10</sup>

In Eqs. (3) through (6),  $\sigma_{23} = 2\rho_s/L_2$  where  $L_j$  is the length of field line in region  $j$ ,  $\beta = 2\rho_s/R$  where  $R$  is the major radius, and  $\sigma_{12} = \rho_s^2 \Omega_i m_i / (L_{\parallel}^2 \eta_{\parallel} e^2)$  is a parallel conductivity coefficient that carries the dimension of density  $n$ , where  $\eta_{\parallel}$  is the parallel resistivity. Note that curvature drive (the  $\beta$  term) is included only in region 1, which we take as the outboard midplane region (OM), and that sheath charge loss (the  $\sigma_{23}$  term) occurs only in region 2, the divertor and X-point region (XP). The sheath loss term  $\sigma_{23} \Phi_2$  in Eq. (5) is a small- $\Phi_2$  approximation to the full nonlinear term, i.e.,  $\sigma_{23}[1 - \exp(-\Phi_2)]$ , that is usually well justified. For simplicity we consider the parallel

lengths of both regions to be identical, i.e.  $L_1 = L_2 \equiv L_{\parallel}$ . The gradients in the two regions are related by the metric tensor of Eq. (2), namely  $\nabla_2 = \mathbf{M}^{-1, \text{tr}} \cdot \nabla_1$ .

To sustain the turbulence against an out-going radial boundary condition on the density flow (Appendix A), it is necessary to replenish the density in the edge region. To that end, we use a restorative density source in the OM:  $S_1(x,y,t) = v(x) \cdot [n_0(x) - n_1(x,y,t)]$ , with reference profile  $n_0(x) = (n_E - n_F) \cdot \frac{1}{2} \cdot (1 - \text{Tanh}[(x-x_0)/\Delta x_0]) + n_F$  and healing rate  $v(x) = v_0 \cdot \frac{1}{2} \cdot (1 - \text{Tanh}[(x-x_0)/\Delta x_0])$ .  $n_E$  and  $n_F$  denote edge and floor densities,  $n_E \gg n_F$ . In the edge region, i.e.,  $x < x_0 - \Delta x_0$ , the source effectively insulates the edge boundary on the “core” side of the simulation ( $x = 0$ ) from the turbulence, while in the SOL,  $x > x_0 + \Delta x_0$ , the healing rate and source are exponentially small and ignorable. A similar expression holds for  $S_2$  in the XP, with healing rate and reference density given by the field-line images of  $v(x)$  and  $n_0(x)$  respectively.

### III. Properties of the model

In paper I, Eqs. (5) through (7), absent dissipation and density sources ( $\mu_{1,2} = D_{1,2} = S_{1,2} = 0$ ), were linearized about a radial density profile,  $n_1(x)$ , and  $\Phi_1 = \Phi_2 = 0$ . The analysis reproduced well-known modes of the edge profile instability in different regimes of collisionality and magnetic geometry. An expression for the ratio of linear mode amplitudes,  $\delta\Phi_2 / \delta\Phi_1$ , Eq. (I.9), was derived, and the extent of electrical disconnection between the two regions, (i.e., the extent to which  $\delta\Phi_2 \ll \delta\Phi_1$  is true) was quantified in the different regimes. We briefly summarize those findings here.

In the regime of low collisionality,  $\sigma_{12}/n > \sigma_{23}$ , the two regions are connected ( $\delta\Phi_2 \sim \delta\Phi_1$ ,  $n_2 \sim n_1 \sim n$ ) and two modes are distinguished that represent different current budgets, depending on wavelength. The longer-wavelength modes are relatively slow-growing, sheath-connected interchange ( $C_s$ ) modes<sup>11</sup> for which the curvature drive in the OM ( $\sim \beta$ ) balances the parallel current flow to the sheath ( $\sim \sigma_{23}$ ) in the XP. At shorter wavelengths, the fanning-enhanced ion polarization current in the XP

$[\nabla \cdot \mathbf{J}_{\text{pol}} \equiv \nabla \cdot (\partial_t \nabla \delta \Phi + \mathbf{v} \nabla^2 \delta \Phi) \sim \delta \Phi^2 k_{\perp}^4]$  tends increasingly to dominate the current budget, i.e., to balance the curvature drive; the modes revert to connected ideal-interchange ( $C_i$ ) magnetohydrodynamic (MHD) modes that are faster-growing than  $C_s$  modes.

It is important to appreciate the role that magnetic geometry (field-line fanning and shear) plays in enhancing the cross-field conductivity in the XP region.<sup>12</sup> For the fastest-growing modes,  $|k_{x1}| \ll |k_{y1}|$  and the field-line transformation, Eq. (4), implies  $k_{x2}^2 \cong \zeta^2 k_{y1}^2$  and  $k_{y2}^2 = k_{y1}^2 / f^2$ : i.e., shear enhances the radial wavenumber and fanning enhances the poloidal wavenumber. It follows that the ion polarization current,  $\nabla \cdot \mathbf{J}_{\text{pol}} \sim \delta \Phi^2 k_{\perp}^4 = \delta \Phi^2 \cdot (k_{x2}^2 + k_{y2}^2)^2$ , is enhanced in the XP by two orders of magnitude, typically, compared to  $\mathbf{J}_{\text{pol}}$  in the OM for the connected modes.

At higher collisionality the regions are disconnected,  $\delta \Phi_2 \ll \delta \Phi_1$ , and again two modes are distinguished, depending on wavelength and corresponding to different current budgets. At longer wavelengths (but shorter than those which characterize the connected regime), we find the resistive X-point (RX) mode<sup>3</sup> for which the curvature-driven current is balanced by the parallel current flowing from the OM to the XP region. The mode is evanescent in the XP and is faster-growing than either of the connected modes. At still shorter wavelengths, the fastest-growing resistive ballooning (RB) mode<sup>2</sup> serves to balance the current drive with the polarization current in the OM; this mode is completely disconnected,  $\delta \Phi_2 = 0$ . See paper I, and references therein, for further details of the linear analysis.

A blob dispersion relation (BDR) was derived in I by using the ‘‘blob correspondence rule,’’  $\text{Im}(\omega) \rightarrow v_x / a_b$ , in the linear dispersion relation (where  $a_b$  is the blob radius). It was found that the BDR prediction of  $v_x$  agreed with simulations of equations (3) through (7) for times short compared to blob instability growth times, i.e., while the blob reasonably retained its initialized circular cross-section. The linear dispersion relation and the BDR are completely specified in terms of two scale-invariant

parameters (obtained from a Connor-Taylor scaling analysis<sup>13</sup>) that characterize the different linear regimes described above, namely

$$\Lambda = n_b \sigma_{23} / \sigma_{12} = v_{ei} L_{\parallel} / \Omega_e \rho_s, \quad \Theta = \hat{a}^{5/2} = (a_b / a_*)^{5/2}. \quad (8)$$

The parameter  $\Lambda$  measures collisionality or resistivity and  $\Theta$  characterizes the scale size of the blob. Here,  $n_b$  is a blob reference density,  $\hat{a} \equiv a_b / a_*$  is a dimensionless and scale-invariant blob radius, and  $a_* = (\beta / \sigma_{23}^2)^{1/5} (= \rho_s^{4/5} L_{\parallel}^{2/5} / R^{1/5}$  in dimensional units). It has been shown by 2D simulations that a sheath-connected blob of radius  $a_*$  is least susceptible to internal blob instabilities.<sup>14</sup>

A regime diagram in  $(\Theta, \Lambda)$  space was presented in Fig. (I.1). The connected modes, described above, are found at  $\Lambda < 1$  for sufficiently large  $\hat{a}$ . Depending on  $\Lambda$ , decreasing  $\Theta$  (or  $\hat{a}$ ) takes the mode or blob from the RX to the RB regime, or from the  $C_s$  to the  $C_i$  regime. A convenient, scale-invariant blob velocity is  $\hat{v} = v_x / v_*$ , where  $v_* = (a_* \beta)^{1/2} (= c_s (a_* / R)^{1/2}$  in dimensional units) is the velocity in the RB regime for the case  $a_b = a_*$ . In this electrostatic model, the blob velocity is bounded by

$$\frac{1}{\Theta^{4/5}} \equiv \frac{1}{\hat{a}^2} < \hat{v} < \hat{a}^{1/2} \equiv \Theta^{1/5} \quad (9)$$

where the lower bound is given by the low- $\Lambda$ , large  $\hat{a}$  (sheath-connected) limit of the BDR, and the upper bound is given by the high- $\Lambda$ , small  $\hat{a}$  (RB) limit.<sup>1</sup>

The correspondence rule and the scalings summarized in this section are in good agreement with prepared blob simulations discussed in I, neglecting magnetic shear [Fig. (I-2)]. In the next section, we first illustrate the role of magnetic shear on blob propagation and then discuss the results of the two region model for simulations of fully developed turbulence.

## IV. Simulations of turbulence

### A. Effect of magnetic shear on blobs

In Figure (1) we illustrate magnetic shear by demonstrating its effect on the propagation of an isolated blob as seen in the OM. (The numerical algorithms and boundary conditions used for these simulations are described in Appendix A.) Compared to the turbulent cases that follow, we have chosen a relatively low value for the parallel resistivity ( $\eta \equiv 1/\sigma_{12} = 10^3$ ) to ensure strong electrical connection between the two regions. In Figs. (1a) and (1b) there is neither magnetic shear nor fanning,  $\xi = 0$  and  $f = 1$  in Eq. (2): the magnetic geometry is off (G: OFF). In Figs. (1c) and (1d) the magnetic geometry is on (G: ON):  $\xi = 4$  and  $f = 1/4$ . ( $1/f \sim \xi$  is typical of experiments, and the values chosen here were limited by the available resolution.) In Paper I, Appendix B, we provide an exact solution of the model equations in the infinite-conductivity ( $\sigma_{12} \rightarrow \infty$ ), perfectly-connected limit, with or without magnetic geometry, that we take as the initial condition in either case here:  $n_1 = 0.01 + \exp[-\rho(t = 0)^2/a_b^2]$  and  $\Phi_1 = (\beta/\sigma_{23})\partial_y \log(n_1)$ , with  $\Phi_2$  and  $n_2$  field line copies of  $\Phi_1$  and  $n_1$ , and where  $\rho$  is defined in Eq. (I.B.19). (The simulation initial condition is the periodic-in- $y$  version of this.) In all cases,  $\beta = \sigma_{23} = 10^{-3}$ . In Fig. 1 (a) and (b),  $Lx_1 = Lx_2 = Ly_1 = Ly_2 = 32\pi$  and  $a_b = 8$ , while  $Lx_1 = Ly_2 = 16\pi$ ,  $Ly_1 = Lx_2 = 64\pi$  and  $a_b = 12$  in Fig. 1 (c) and (d). The numerical grid is  $256 \times 256$  in both regions, so  $f = \Delta x_1/\Delta x_2 = \Delta y_2/\Delta y_1$ , the ratios of grid spacings. (We discuss the numerical implementation of the field-line mapping between the two regions in Appendix B.) The diffusion coefficients of vorticity and density are  $\mu_{1,2} = D_{1,2} = 0$  in each case, and there is no restorative density source,  $S_{1,2} = 0$ .

On the infinite spatial domain, the Gaussian density blob initial condition (given above) yields an initial *radial* velocity ( $-\partial_y \Phi_1$ ) that is simply proportional to the inverse square of the blob radius,  $v_x \sim 1/a_b^2$ , at all points in the OM. This is the sheath-connected velocity scaling of the original blob model.<sup>15</sup> There is no *poloidal* motion with the magnetic geometry off. The exact solution with the magnetic geometry on (i.e., magnetic

shear and X-point fanning) is a sheared Gaussian in the OM that moves radially outward *and poloidally downward* with uniform velocity on the infinite domain. However, for the periodic boundary conditions of the simulations,  $n_1$  is initially a superposition of Gaussians centered in infinitely many image domains, and the corresponding initial  $\Phi_1$  is a dipole field that straddles this density blob in our simulation cell. The velocity field is non-uniform across the blob (the contours of  $\Phi_1$  are streamlines of the flow), and the blob is distorted into the familiar crescent shape upon propagating, as seen in Figs. (1b) and (1d). It is apparent that *magnetic field line shear induces poloidal velocity* in isolated blob propagation in the periodic-domain case as well. Field-line shear is one mechanism that may account for the poloidal blob motion often observed in experiments.<sup>16</sup>

Notice that the flows in Fig. (1) circulate density from the crescent wings into the backside of the blob, faster than the central part of the blob is advancing. In the edge region, where the ambient radial density gradient is negative, this local blob flow tends to draw out a “streamer”: a poloidally localized density channel flowing out into the SOL, as will be seen in the next section. We find that streamers are the general rule for blobs born from the profile instability in the present model (and in other simulations without sheared flow<sup>17</sup>), and we now turn our attention to this situation.

### **B. Effect of collisionality and X-point geometry on turbulence**

In this section, we compare four simulations chosen to contrast the effects of collisionality (HIGH or LOW) and X-point geometry (ON or OFF). The parameters of the simulations are as follows. (All variables and parameters are dimensionless, with physical units given in Sec. II.)  $L_{x_1} = 16\pi$ ,  $L_{y_1} = 64\pi$ , with  $L_{x_2} = L_{x_1}/f$  and  $L_{y_2} = L_{y_1}f$ , where  $f$  is the fanning parameter defined in Eq. (2). The numerical grid is  $256 \times 256$  in both regions, so  $f = \Delta x_1/\Delta x_2 = \Delta y_2/\Delta y_1$ , the ratios of grid spacings. For the fanned and sheared cases, “geometry on” (G: ON), displayed in Figs. (2a) and (2b), we take  $f = 1/4$  and  $\xi = 4$ . For the two cases without fanning and shear, “geometry off” (G: OFF), in

Figs. (2c) and (2d),  $f = 1$  and  $\xi = 0$ . (We discuss the numerical implementation of the field-line mapping between the two regions in Appendix B of this paper.) In all cases,  $\beta = \sigma_{23} = 10^{-3}$ . For low resistivity cases ( $\eta$ : LOW), Figs. (2a) and (2c), we use  $\eta \equiv 1/\sigma_{12} = 10^4$ , and  $\eta = 10^5$  for the high resistivity cases ( $\eta$ : HIGH), Figs. (2b) and (2d). The diffusion coefficients of vorticity and density are  $\mu_{1,2} = D_{1,2} = 10^{-2}$  in all cases. The OM initial conditions are  $n_1(x,y) = n_0(x) + \delta n(x,y)$  and  $\Phi_1(x,y) = 0$ , where  $n_0(x)$  is the reference profile given in Sec. II, and we take  $x_0 = Lx_1/4$ ,  $\Delta x_0 = 10 \Delta x_1$ ,  $n_F = 0.01$  and  $n_E = 1.0$ , effectively normalizing density to the physical value at the edge boundary ( $x = 0$ ).  $\delta n$  is a spatially random perturbation between 0 and 0.01. The XP initial conditions are field-line copies of those in the OM, but with a different random sequence for  $\delta n$ .

The assumption (used here for simplicity) of constant  $\sigma_{23}$  has important consequences for the simulations. Other work on turbulent momentum transport<sup>18</sup> has shown that the sheath provides a momentum sink that damps sheared flow, and that a sheared flow layer in the edge plasma modifies the blob creation process. The interplay of sheared flows (which can stabilize the turbulence in some regimes) and density profile modifications due to blob ejection is a complicated and fascinating subject which we shall defer to future publications, focusing here instead on the effects of magnetic geometry and collisionality. Suffice it to say that we expect that the radial streamers seen in the simulations described here would have been more blob-like if we had set  $\sigma_{23} = 0$  inside the edge plasma near  $x = x_0$ .

In Figure (2) we present snapshots of the density in the OM for the four simulations. The four snapshots in Fig. (2) are taken at a time,  $t = 1200$ , much larger than the e-folding times of the fastest growing modes: 50 in (a) and (c), 43 in (b) and (d).<sup>19</sup> It is clear that the profile instability gives birth to streamers or blobs that propagate into the SOL and that blob radial velocity is significantly greater in the high resistivity cases than in the low resistivity cases; compare (a) to (b) and (c) to (d). This is consistent with previous observations, particularly the BOUT simulations<sup>8</sup> that inspired the present study,

in which transport was found to increase with collisionality. But Fig. (2) also suggests that magnetic geometry (field-line fanning and shear) retards the development of blobs from the instability and reduces the radial velocity of blobs in the SOL; compare (a) to (c) and (b) to (d).

A “bloblet analysis” allows us to isolate those structures which dominate the turbulent radial flux, i.e., the blob-streamers in Fig. (2). Here and henceforth a blob is, by definition, a density fluctuation for which there exists a Gaussian function that is a sufficiently good local approximation in  $y$  to the fluctuation. Our analysis and goodness-of-fit criterion are discussed further in Appendix C.

In Figure (3) we plot  $\Phi_2$  versus  $\Phi_1$  for blobs detected at  $x = 30$  in the OM for the four turbulence simulations. Each dot in the figure represents one blob, and the entire duration of each simulation is represented [ $\Delta t = 20,000$  in (a) and 10,000 in (b)–(d)].  $\Phi_1$  is measured at the center of the bloblet, and  $\Phi_2$  is measured at the field-line image point in the XP. This gives us a measure of electrical connection between the two regions, with perfect connection corresponding to the identity line. Clearly *collisionality disconnects the two regions*: the cases of low resistivity, (a) and (c), are connected compared to those of high resistivity, (b) and (d).

In each case, the blobs are approximately distributed about a straight line through the origin, with some dispersion about that line. This is to be expected particularly in the sheath-connected limit: the parallel current balances the sheath current, the right-hand side of Eq. (5) is zero, and (ignoring diffusion)  $\Phi_2 / \Phi_1 = (1 + \sigma_{23} n_2 / \sigma_{12})^{-1} \sim 1 / (1 + \Lambda)$ . In this limit,  $\Phi_1$  and  $\Phi_2$  are highly correlated, with fluctuations in the XP blob density,  $n_2$ , providing dispersion about a line whose slope approaches unity, from below, in the limit of zero resistivity ( $\sigma_{12} / n_2 \rightarrow \infty$ ) and become less connected (and de-correlated) as the resistivity increases.

The nonlinear polarization currents couple the potentials *across* field lines,  $\nabla \cdot \mathbf{J}_{\text{pol}} \sim k_{\perp}^4$ , and are responsible for instability (Kelvin-Helmholtz)<sup>20</sup> and turbulent mixing

(cascading) in the *separate* regions. Therefore the potentials are expected to be increasingly uncorrelated as  $\mathbf{J}_{\text{pol}}$  dominates the current budget in either region. The magnetic geometry enhances cross-field conductivity in the XP region.<sup>8,12</sup> In particular, the streamers of Fig. (2) have  $k_{y1}^2 \gg k_{x1}^2$  so that  $\sigma_{\perp 2} \sim k_{\perp 2}^2 \cong k_{\perp 1}^2 \cdot (\xi^2 + 1/\Gamma^2)$ , implying  $\sigma_{\perp 2} / \sigma_{\perp 1} \cong 32$  for the cases with magnetic geometry on, Figs. (3a) and (3b). Thus by amplifying the nonlinear, mixing polarization current in the XP, *magnetic geometry de-correlates  $\Phi_1$  and  $\Phi_2$*  as seen by comparing Figs. (3b) and (3d).

One way to quantify the collisional disconnection and geometric de-correlation discussed here is to use the Pearson measure of correlation; taking the inner products of the datasets we find that  $\delta\Phi_1 \cdot \delta\Phi_2 / (\delta\Phi_1 \cdot \delta\Phi_1 \delta\Phi_2 \cdot \delta\Phi_2)^{1/2} = (0.996, 0.867, 0.999, 0.958)$  for the blob data in cases (a, b, c, d) of Fig. (3).

Figures (2) and (3) are consistent with the blob “circuit diagram” picture.<sup>21</sup> Recall that in the blob model of turbulent transport,<sup>15</sup> the poloidal gradient of the density in Eq. (3) drives dipole charge separation across the blob, and the resulting  $\mathbf{E} \times \mathbf{B}$  drift propels the blob radially outward in the OM. This charge polarization mechanism is essentially the Rosenbluth-Longmuir mechanism<sup>22</sup> for the linear interchange instability, applied here to the density contours of the blob to obtain the nonlinear transport. To obtain a complete picture of all the blob parameter regimes, this classic blob model needs to be viewed dynamically in terms of charge flow (current); the curvature-driven current in the blob is fixed by the driving force, and the net blob potential responsible for the  $\mathbf{E} \times \mathbf{B}$  motion is proportional to the net resistance in the blob circuit, which depends on the collisionality and geometry.<sup>21</sup>

Of the four turbulence simulations, the case of low- $\eta$  and magnetic geometry on (a) offers the path of least resistance to current flow, both along field lines and across field lines in the XP, and produces the slowest blobs. With the geometry off (c), the resulting drop in cross-field conductivity shifts current loop closure to the sheath; the resistance is increased, and the blobs speed up. In the high- $\eta$  cases, (b) and (d), the two

regions are relatively disconnected. With the magnetic geometry off (d), the polarization current in the OM provides the path of least resistance and, because this is the most resistive such path of all four cases, the fastest blobs are produced. Turning the geometry on (b) slows down the blobs, again, due to enhanced cross-field conductivity in the XP. To summarize: *magnetic geometry reduces blob velocity, while collisionality increases it.* The density flux, which we examine next, behaves similarly.

In Figure (4a) we plot the poloidally-averaged radial particle flux,  $\langle \Gamma \rangle_y = \langle n \cdot v_x \rangle_y$ , measured at  $x = 30$  in the OM, as a function of time for the four simulations, and the probability distribution function (PDF) of  $\Gamma$  for all  $y$  and  $t$ , at  $x = 30$ , in Fig. (4b). Temporal intermittency is observed in all cases, though in the low- $\eta$ , geometry-on case (dash-dotted), the intermittent bursts occur on a much longer time scale than in the other three cases and are of much smaller amplitude. This data is measured at a point and so resembles the experimental “probe” data<sup>23-26</sup> that measures ion saturation current ( $I_{\text{sat}}$ ) at a point in the tokamak SOL. As seen in Fig. (4b), the PDFs of flux for all four simulations are similar, and thus *insensitive to collisionality and geometry*, when plotted against flux normalized by standard deviation,  $\sigma_\Gamma$ , as are those of the experimental data (with respect to  $\sigma_{I_{\text{sat}}}$ ) across several machines which differ greatly in their geometry and underlying physics.<sup>24</sup> All PDFs are strongly skewed to positive  $\Gamma$  ( $I_{\text{sat}}$ ) with exponential tails, consistent with the universal, non-diffusive mechanism (blob dynamics) underlying the observed transport. The presence of a positive tail and the absence of sensitivity to detailed parameters in the PDFs are important points of agreement between the two-region model turbulence simulations and the experimental data. In fact, the PDFs in Fig. (4b) are nearly identical to the ones measured experimentally in Ref. 24. On the other hand, such agreement, while necessary, is hardly sufficient to validate the present model. The (numerically and experimentally) observed insensitivity of the PDFs show that this statistical measure reveals little about the underlying physical processes.

The same charge polarization mechanism that propels positive density fluctuations radially outward moves density depressions radially inward. In the nonlinear regime, “holes” move backwards toward the core,<sup>27</sup> accounting for the relatively weak negative flux recorded in Fig. (4b). Holes occur in the wakes of isolated blobs and are produced in blob-blob interactions. See Figs. (1) and (2).

The poloidally and temporally averaged density profiles in the OM,  $n(x)$ , are displayed in Fig. (5a), the logarithmic derivative of these profiles in Fig. (5b), and the skewness  $S(x)$  of the density fluctuations in Fig. (5c) for the four simulations. ( $S = \langle (n(x,y,t) - \langle n \rangle_{y,t})^3 \rangle_{y,t} / \sigma^3$ , where  $\sigma$  is the standard deviation of the density fluctuations, indexed by  $y$  and  $t$ , at a fixed value of  $x$ .) First, we observe in Fig. (5a) that in all four cases the strong turbulent radial particle flux creates a two-scale density profile with a nearly-constant density shelf extending into the far SOL as a result of the blob convection. The magnitude of the far-SOL density in the four simulations is proportional to the convective particle flux in each case [compare with Fig. (4a)]. As an aside we mention that a parallel particle loss term was not included in the OM continuity equation, which restricts validity of the model to cases in which the convective radial transport is much faster than the parallel sonic flow.

The second important result in Fig. (5) is that the radial location of the maximum of the logarithmic density gradient,  $-d(\ln n)/dx$ , for each of the four simulations [Fig. (5b)] coincides with the location where the skewness  $S$  of the density fluctuations vanishes [Fig. (5c)]. As seen from the density profile in Fig. (5a), this point also marks the transition between the sharp-gradient (diffusive) and weak-gradient (convective) turbulent particle transport regions, and thus is correlated with the blob generation zone. The correlation of blob generation with the maximum logarithmic pressure gradient has also been observed experimentally using the gas-puff-imaging diagnostic.<sup>28,29</sup> These features lead to a consistent physical picture of blob formation, which we now discuss.

Experimental data and simulations indicate that the density blobs arise from the nonlinear saturation of linear instabilities at the plasma edge. For example, curvature-driven blobs tend to arise near the maximum of the linear growth rate, or equivalently, of  $-d(\ln n)/dx$  for interchange and ballooning modes. We refer to this radial location as the “birth zone” of the blobs. The small initial positive and negative density perturbations of the interchange mode grow and eventually disconnect as part of the turbulent saturation process, forming blobs and holes, respectively. (The exact saturation mechanism is thought to depend on profile modification, wave-breaking, sheared flow generation and nonlinear cascades, depending on regime.) At this point the Rosenbluth-Longmuir charge-polarization mechanism, which was driving the linear instability, causes the coherent objects to move: the positive-density blobs move outwards and the negative-density holes move inwards. Since the blobs and holes are emitted intermittently, one would expect that their creation and propagation should be reflected in the higher statistical moments, e.g. in the skewness  $S$ . As seen in Fig. (5), the statistical analysis of the turbulent fluctuations in the present simulations supports this picture. In each case, we find that  $S(x)$  changes sign near the point of maximum linear growth rate:  $S = 0$  in the birth zone (reflecting the equal number of blobs and holes created by the interchange nature of the underlying instability),  $S < 0$  in the direction of hole propagation (up the magnetic field and density gradients), and  $S > 0$  in the direction of blob propagation (down the magnetic field and density gradients). The identification of the blob birth zone with the location where  $S = 0$  is also supported qualitatively by experimental data on several machines<sup>26, 28, 30, 31</sup> and by previous simulations<sup>32</sup> that observe a skewness profile very similar to the one obtained here.

These observations motivate the following decomposition of the turbulent flux into components that characterize the blob transport. We take  $S(x_b) = 0$  to define the radial location of blob birth,  $x_b$ , and measure the blob *birth density* there,  $n_b = n(x_b)$ . We write the averaged density as  $n(x) = f_p(x)n_b$ , and define the blob *packing fraction*  $f_p(x)$ ,

which is related to the blob creation rate as follows. If all blobs have density  $n_b$ , then  $f_p$  measures the mean blob duty cycle ( $0 < f_p < 1$ ): the average blob duration at a fixed point divided by the mean time between blob arrivals at that point. However, the blobs are absorbed by diffusion and fragment as they propagate, so that  $f_p$  more generally provides a lower bound of the duty cycle. (Previous analyses of turbulence data on a reversed field pinch<sup>33</sup> and NSTX<sup>34</sup> used a definition of the packing fraction very similar to the one used here.) We measure the poloidally and temporally averaged radial flux,  $\bar{\Gamma}(x) = \langle \Gamma \rangle_{y,t}$ , from the simulations and define the flux-weighted average blob velocity in the obvious way:  $\bar{v}_x(x) = \bar{\Gamma}(x)/n(x)$ , or  $\bar{\Gamma}(x) = f_p(x) n_b \bar{v}_x(x)$ .

The average flux,  $\bar{\Gamma}$ , and its three components ( $\bar{v}_x$ ,  $f_p$ ,  $n_b$ ), measured at  $x = 30$ , are recorded in Table I for the four simulations. (We refer to this as “probe data” for the simulation because the measurements are made at a point in the SOL and hold no information about the geometrical properties of the blobs, such as cross section,  $a_y$ , and particle transport rate,  $a_y \Gamma$ , that are available from the bloblet analysis described above.) From Table I, we see that the flux increases by a factor of 30 in going from the most connected case (a) to the least connected case (d) and that most of this increase is due to the 6-fold increase in the blob velocity,  $\bar{\Gamma}/n$ , with a 3-fold increase in the packing fraction and a relatively modest increase in the birth density  $n_b$ . In comparing the other cases we see that this is generally true: *much of the change in flux results from changes in the average blob velocity*, with the packing fraction playing a secondary role.

This is an interesting and important result which will require verification or extension to more general situations where the blob generation rate (or packing fraction) may be controlled by physics not in the present model, e.g. sheared flows or other regulation mechanisms which can make the edge gradients marginal. In the present context of robustly unstable edge plasma, the implication is that the part of the blob flux that is understood analytically (the velocity scaling) is more important than the part that

must be computed by a code (the packing fraction). Ultimately, it will be desirable to have a general predictive theory of the scaling of the total flux.

The trends observed in the flux-weighted probe velocity are echoed in the blob data. In Table I we record the average radial velocities of blobs for which the particle transport rate,  $a_y \Gamma$  is positive. A 7-fold increase in blob velocity is observed in going from case (a) to case (d), compared to the 6-fold increase for the probe data, and again the intermediate cases are indistinguishable. This agreement between the blob velocities and flux-weighted probe velocities supports the conclusion that the scaling of the turbulence is dominated by blob physics.

The cases of intermediate flux, (b) and (c), are fairly indistinguishable with respect to flux, velocity and packing fraction, consistent with the near-perfect overlap of their average density profiles in Fig. (5a). Case (b) has higher conductivity across field lines in the XP, thanks to the magnetic geometry, but relatively low parallel conductivity due to higher collisionality. Case (c) represents the opposite situation: high parallel conductivity and low cross-field conductivity. Apparently the respective paths of least circuit resistance are similarly conducting and interchangeable with respect to blob dynamics in the two cases.

### C. Bloblet analysis

We have also calculated the PDFs of  $H \equiv a_y \Gamma$ , the particle transport rate by an individual blob. ( $a_y$  is the poloidal half-width. See Appendix C.) We find that the PDFs of  $H$  are similar to those of particle flux obtained from the probe data. For example, 40% of the total positive  $H$  is found at  $H > 2\sigma_H$ , with a similar fraction of the total positive particle flux at  $\Gamma > 2\sigma_\Gamma$  from the probe data, consistent with experimental results<sup>35</sup> and other simulations.<sup>36</sup> These high- $H$  blobs rarely occur, comprising less than 10% of the blob population in each simulation. They contribute so much to the total  $H$  budget because their high velocities more than compensate for their infrequent occurrence.

We define a mean particle transport rate,  $f_p n_b \langle v_x \rangle \langle a_y \rangle$ , analogous to the mean flux used in the probe data analysis, where the averages may be restricted to a filtered subset of the blob collection in each simulation, e.g.,  $H > 0$ ,  $H > \sigma_H$ ,  $H > 2\sigma_H$ , etc.<sup>37</sup> Consistent with the flux data,  $H$  increases with disconnection for all thresholds, and the increase is dominated by the increase in radial velocity, as for the probe flux data. Comparing the most connected, lowest- $H$  case (a) to the most disconnected, highest- $H$  case (d), we observe a 9-fold increase in  $H$  dominated by a 7-fold increase in radial velocity, at the highest threshold ( $2\sigma_H$ ). Packing fraction and birth density increase by 60%, whereas blob width,  $\langle a_y \rangle$ , decreases by a factor of 2 with disconnection.

In Figure (6a) we plot the *average* blob radial velocity versus  $a_y$  for the four simulations, with  $v_x$  and  $a_y$  normalized to  $v_*$  and  $a_*$  respectively. (See Sec. III.) The data has been filtered by requiring  $H > 0$  of each blob. The average blob collisionality parameters,  $\langle \Lambda \rangle$ , for the four simulations are listed in the final column of Table I. With reference to the blob regime diagram [Fig. (1) of Paper I], we find that the most disconnected, highest- $H$  blobs (high- $\eta$ , G: OFF) are largely in the resistive ballooning (RB) regime; a greater fraction are found in the resistive X-point (RX) regime with the geometry on (high- $\eta$ , G: ON); and for low- $\eta$  the blobs are in the connected-sheath and connected-interchange regimes ( $C_s$ ,  $C_i$ ), as expected.

Asymptotic velocity scalings inferred from the blob dispersion relation, c.f. Sec. III, are indicated by solid lines in Fig. (6a) for the RB and  $C_i$  regimes ( $v_x \sim \hat{a}_y^{1/2}$ ) and for the RX and  $C_s$  regimes ( $v_x \sim \hat{a}_y^{-2}$ ). The blob data clusters loosely about these curves but does not lie on them, and the largest observed velocities exceed the theoretical upper bound for circular (i.e. isotropic) blobs of  $\hat{v}_x = 1$  for small  $\hat{a}$ . The scalings are based on *strong* inequalities (Paper I, Sec. III) imposed on the BDR that are not satisfied by the data, in general. But perhaps more telling, in some cases, is the assumption of blob isotropy implicit in the BDR.

The blob data analysis is, of course, very sensitive to filtering, indeed to the definition of a “blob” itself. For example, in Fig. (6b) we plot the velocity versus width of *individual* blobs, filtered by requiring that each represent a local maximum in  $x$ , as well as  $y$ . These are the roundest blobs in our collection of *thousands* of blobs in total, and are arguably closest to satisfying the assumption of blob isotropy,  $a_x = a_y$ . It is clear that the vast majority of blobs are not local  $x$ -maxima; they are (poloidal slices of) streamers, and they are moving about twice as fast as anticipated for *isotropic* blobs of width  $a_y$ , in the most disconnected (high- $\eta$ , G: OFF) case. This speed-up is apparently due to streamer geometry, as we now show.

In the strongly disconnected (RB) limit, the polarization current balances the curvature-driven current source in the OM. Assuming  $\partial_x \sim 1/a_x$ ,  $\partial_y \sim 1/a_y$  and equating the convective derivative of vorticity to the curvature drive term ( $\sim\beta$ ) in Eq. (3), we find the velocity scaling  $v_x = v_{x0} (a_x/a_y)^{1/2} / (1 + a_y^2/a_x^2)^{1/2}$ , where  $v_{x0} = (\beta a_y)^{1/2}$ . For streamers, an aspect ratio ( $a_x/a_y$ ) of 4 increases  $v_x$  by a factor of approximately  $2^{3/2}$  over the isotropic case, more consistent with the present simulations.

A recent analysis of gas-puff-imaging data shows that the blobs observed experimentally in the SOL tend to be isotropic and their radial velocity to be bounded by  $\hat{v}_x = 1$ .<sup>18,29</sup> As mentioned earlier, simulations not discussed here<sup>18</sup> indicate that the radial streamers tend to be broken up into more isotropic structures when a velocity shear layer is allowed near  $x = x_0$  (by turning off the sheath conductivity there,  $\sigma_{23} = 0$ ). This is also supported by the simulation results of other groups<sup>38</sup> Thus, future extensions of the bloblet analysis with the two-region model will include the effects of a velocity shear layer near the edge plasma.

## V. Conclusions

Using a unique two-region simulation model, introduced in Paper I of this series and summarized in Secs. II and III, we have studied turbulent transport by blobs, driven

by the pressure gradient instability in the outboard midplane, as a function of electrical connection with the X-point region of a diverted tokamak.

The model used in paper I was generalized here to include magnetic shear along the field lines, and was applied to simulate isolated blob propagation in Sec. IV A. It was shown that magnetic shear induces poloidal velocity in isolated blobs in the low-collisionality regime.

In the turbulence regime (discussed in Secs. IV B and C), we demonstrated a number of results using the two-region model simulations:

(1) The particle flux increases with collisionality but is reduced by magnetic field-line fanning and shear. We argued that this is consistent with the circuit diagram picture<sup>9</sup> underlying blob dynamics. Magnetic geometry dramatically enhances cross-field conductivity in the X-point region, slowing down the blobs, but it also de-correlates the electrostatic potential fluctuations in the two regions, as noted previously,<sup>8,39</sup> and supports the proposal to use turbulent transport to spread the divertor heat load without affecting the core and OM SOL plasmas.<sup>40</sup>

(2) The PDFs of flux that we measure in the simulations, like the PDFs of probe saturation current measured in experiments, are *insensitive* to the details of the plasma parameters (here, collisionality and magnetic geometry); all the PDFs overlap when plotted as functions of flux normalized by standard deviation. They are strongly skewed to positive flux with exponential tails underscoring the non-diffusive, ballistic (blob) nature of the transport.

(3) We observed that the skewness of the density fluctuations passes through zero at the radial location where the turbulent profile instability growth rate is maximized, in each simulation, and we identified this location with the birth zone of the blobs. Decomposing the flux into the product of birth-zone density, packing fraction and radial velocity, we showed that increases in flux in all cases, whether due to increased collisionality or the absence of field line fanning and shear, are affected both by increases

in blob velocity, and increases in packing fraction (or equivalently, rate of blob production) with the former playing a somewhat more important role. A bloblet analysis of particle transport rate,  $a_y \Gamma$ , led to similar conclusions.

(4) The bloblet analysis was used to explore the dependence of the blob velocity on the poloidal blob width for comparison with theoretical scalings. The data clusters approximately where expected, with scalings predicted by the BDR best supported in the sheath-connected regime. The large velocities ( $\hat{v}_x > 1$ ) observed in the disconnected resistive-ballooning regime were shown to be caused by the elongation of the radial streamers.

This study clearly demonstrates the value of reduced numerical modeling in identifying the essential physics underlying edge and SOL transport phenomena. It is anticipated that straightforward extensions of the model to simulate closed field-line physics, and to include sheared flow and temperature evolution will yield new physics results to aid in the interpretation of 3D turbulence simulations and experiments.

### **Acknowledgments**

This work was supported by the U.S. Department of Energy (DOE) under grant DE-FG02-97ER54392; however, such support does not constitute an endorsement by the DOE of the views expressed herein.

### **Appendix A: Time-advancing algorithm and boundary conditions**

The overall algorithm is split-step, with each term in Eqs. (3) – (7) used to advance the fields in succession. For example, we advance Eq. (3) as follows. Given the charge density (negative vorticity),  $\rho_1 \equiv -\nabla^2 \Phi_1$ , at  $t = 0$ , we (a) explicitly update it with the source term,  $\rho_1(a) = \rho_1(0) + \Delta t \cdot \beta \cdot \partial_y n_1(0)$ , and solve Poisson’s equation for  $\Phi_1(a)$ . Next we (b) advance  $\rho_1(a)$  (and  $\rho_2(0)$ ) using the parallel current term with an explicit, staggered two-step method that may be iterated with a reduced local time step to achieve

stability. With  $\rho_1(b)$  as the initial field, we (c) solve the convection equation,  $\partial_t \rho_1 + v_1 \cdot \nabla \rho_1 = 0$ , using the velocity at the top of the time loop,  $v_1(0)$ . With this result,  $\rho_1(c)$ , as initial condition, we (d) solve the diffusion equation,  $\partial_t \rho_1 = \mu_1 \nabla_1^2 \rho_1$ . This gives us the vorticity at the end of the time loop,  $\rho_1(t = \Delta t)$ , where each step, (a) – (d), uses the time increment  $\Delta t$ . The other fields are similarly updated, and the loop is repeated, etc.

Convection of all fields, as in (c) above, is by the (bi-directional, “phoenical”) SHASTA algorithm with two-dimensional flux limiter due to Zalesak.<sup>41</sup> In benchmarking exercises that recovered linear growth rates to our satisfaction, we confirmed the well-known result that this flux-corrected transport algorithm significantly reduces the numerical dissipation found in simpler algorithms (e.g., Lax-Wendroff). Furthermore, the algorithm resolves the formation of steep fronts, and cascading to high vorticity, without apparently generating spurious (Gibbs) oscillations. Positivity of density under convection is assured, provided a Courant-like constraint is satisfied,  $|v|\Delta t/\Delta x < 1/2$ , which limits the time step used in the simulations in practice.

The diffusion equation for each field, e.g., step (d) above, is solved by the bi-directional, implicit Crank-Nicholson algorithm,<sup>42</sup> and Poisson’s equation is solved by Fourier analysis with cyclic reduction (FACR).<sup>43</sup>

The model equations are solved with continuously periodic boundary conditions in  $y$ . We hold  $\Phi_{1,2}$  and  $\nabla^2 \Phi_{1,2}$  equal to zero at the radial ( $x$ ) boundaries. At the edge boundary ( $x = 0$ ),  $n_1$  and  $n_2$  are held equal to unity, establishing the edge boundary density at  $t = 0$  as the unit of density. The radial gradient of  $n_{1,2}$  is also held equal to zero at the edge boundary, so the density flux is zero there.

Elementary out-going boundary conditions at  $x = L_x$ , for the convection algorithm, produced unacceptably large charge fluctuations at that boundary. In an attempt to cure this, we introduced an artificial out-going flow in a neighborhood of the boundary. In this boundary layer, the radial velocity used in the convection algorithm is interpolated between the self-consistent radial velocity ( $-\partial_y \Phi_{1,2}$ ) and a constant positive

“Hoover” velocity,  $v_H$  (typically  $\frac{1}{4} \Delta x/\Delta t$ ), where the interpolation is weighted increasingly to  $v_H$  as the boundary is approached, as follows:  $v_x = v_H + (-\partial_y \Phi(x,y) - v_H)(L_x - x)^2 / (L_x/8)^2$ , for  $\frac{7}{8} \leq x/L_x \leq 1$ , in both regions. ( $v_y = \partial_x \Phi(x,y)$  everywhere.) This produces a strong out-going flow in the SOL boundary layer, apparent in Fig. (5a), and eliminates the problem of large charge fluctuations at the boundary in the present simulations.

## Appendix B: Field line fanning and shear

Field-line fanning distinguishes the representation of spatial gradients on the Cartesian grids in the two regions and is trivially accommodated. For example, the Poisson equation solver can be called with different grid point spacings  $(\Delta x, \Delta y)$ . If it is called with spacings  $(\Delta x_1, \Delta y_1)$  in region 1, then it is called with spacings  $(\Delta x_2, \Delta y_2) = (\Delta x_1/f, \Delta y_1 \cdot f)$  in region 2. The partial time steps are similarly flexible, e.g., the convection algorithm is called with grid spacings and velocities (gradients of  $\Phi_{1,2}$ ) appropriate to the region at hand.

Magnetic field-line shear affects only the parallel current terms ( $\propto \sigma_{12}$ ) in Eqs. (3) and (5), where  $\Phi_1$  and  $\Phi_2$  are differenced on the same magnetic field line in their respective regions, consistent with the field-line mapping, Eq. (2). But the Cartesian grid labels for a field line are different in the two regions. A field passing through grid point  $(i_1, j_1)$  in region 1 passes through  $(i_2, j_2)$  in region 2, where  $i_2 = i_1$ , and  $j_2 = j_1 + \xi_G \cdot (i_1 - 1)$ , modulo  $n_y$  – due to the periodic boundary conditions in  $y$  in both regions. [We use the same grid dimensions  $(n_x, n_y)$  in both regions.] The grid shear,  $\xi_G$ , must be an integer and so restricts the spatial shear,  $\xi = \xi_G \cdot \Delta y_2 / \Delta x_1$  in Eq. (2), to discrete values on a given numerical grid. With periodic boundary conditions, the shear maps straight radial lines in region 1 ( $y_1 = \text{constant}$ ) onto a series of parallel slanted lines in region 2, i.e., a “barber pole” pattern.

## Appendix C: Bloblet analysis

The one-dimensional “bloblet” basis set consists of Gaussians in the poloidal variable ( $y$ ) parameterized by location ( $y_0$ ) and width ( $a_y$ ):

$$B = \left\{ b(y; y_0, a_y) = \exp[-(y - y_0)^2 / 2a_y^2] \mid 0 \leq y, y_0 \leq L_y, \Delta y \leq a_y \leq L_y / 4 \right\}.$$

At any given time  $t$ , a poloidal slice (nominally at  $x = 30$ ) through the density in the OM reveals bumps in  $y$ . A bump is judged to be a blob only if it is well-approximated locally by one of the bloblets. The goodness of the approximation is defined to be the normalized inner product between the bloblet and the density,

$$\text{goodness}(y_0, a_y, t) = n_1 \cdot b / \sqrt{(n_1 \cdot n_1)(b \cdot b)},$$

where  $n_1 \cdot b \equiv \int n_1(x, y, t) b(y; y_0, a_y) dy$  and  $n_1 \cdot n_1 \equiv \int n_1(x, y, t)^2 dy$ , and the integral is the discrete numerical version: a sum over the poloidal grid. Notice that this measure of goodness is independent of the amplitudes of  $n_1$  and  $b$ . Although technically the Gaussian is not a wavelet, because it does not oscillate and have zero mean in  $y$ , its derivative does satisfy those conditions, so this Gaussian-fitting procedure is closely related to the continuous wavelet transform method.<sup>44</sup>

The goodness threshold that we have adopted for all simulations in this paper is 0.9: the set  $\{y_0, a_y, t\}$  is added to the blob collection, for a given simulation, only if  $\text{goodness} \geq 0.9$ . We also demand that  $y_0$  be a local maximum in  $y$  of  $n_1(x, y, t)$  and that there be at most one blob at  $(y_0, t)$ : that of the greatest goodness with respect to  $a_y$ . Once a blob has been identified, various measurements are taken at  $(x, y_0, t)$ , e.g.,  $v_x, v_y, n_1, \Phi_1, \Phi_2$ , etc., and the enhanced set,  $\{y_0, a_y, t, v_x, v_y, n_1, \Phi_1, \Phi_2, \dots\}$ , is appended to the blob *structure* for subsequent diagnosis.

**Table I.** Results of the four turbulence simulations. From the “probe” data at  $x = 30$ : temporally and poloidally averaged particle flux,  $\bar{\Gamma}$ , mean radial velocity,  $\bar{\Gamma} / n$ , and packing fraction,  $f_p = n / n_b$ . The (dimensionless) density in the blob birth zone,  $n_b$ , is defined to be the density at the radial location where the skewness  $S$  of the density fluctuations vanishes. (The unit of density is that at the edge boundary,  $x = 0$ , and the unit of flux is that density times  $c_s$ .) From the blob data at  $x = 30$ : average radial velocity,  $v_x$ , divided by  $v_*$ , and average collisionality parameter,  $\Lambda = n_1 \cdot \sigma_{23} / \sigma_{12}$ , for blobs at  $x = 30$ . The blob data is restricted to blobs of positive particle transport rate ( $a_y \Gamma$ ); the probe data is not restricted.

Simulation Case	$\bar{\Gamma}$ Probe	$\bar{\Gamma} / n$ Probe	$f_p$ Probe	$n_b$	$\langle v_x \rangle / v_*$ Blob	$\langle \Lambda \rangle$ Blob
(a) G: ON $\eta$ : LOW	$2.5 \times 10^{-4}$	$4.2 \times 10^{-3}$	0.21	0.28	0.14	0.095
(b) G: ON $\eta$ : HIGH	$3.0 \times 10^{-3}$	$1.9 \times 10^{-2}$	0.41	0.38	0.50	2.6
(c) G: OFF $\eta$ : LOW	$2.8 \times 10^{-3}$	$1.8 \times 10^{-2}$	0.43	0.37	0.49	0.24
(d) G: OFF $\eta$ : HIGH	$7.5 \times 10^{-3}$	$2.5 \times 10^{-2}$	0.65	0.46	0.96	3.9

## Figure Captions

**Fig. 1.** (Color online) Isolated blob evolution as seen in the OM:  $n_1(x,y)$  (grayscale or color) and  $\Phi_1(x,y)$  (contour lines). (a) The initial condition with no fanning ( $f = 1$ ) and no shear ( $\xi = 0$ ), i.e., no “geometry” (G: OFF). The initial condition in the XP is a field-line copy of that in the OM. (b) The isolated blob in (a) evolved to  $t = 200$ . (c) The isolated blob initial condition with shear and fanning:  $\xi = 4$  and  $f = 1/4$  (G: ON). (d) The isolated blob in (c) evolved to  $t = 200$ . Note that magnetic shear induces poloidal velocity ( $v_y < 0$ ) in blob propagation.

**Fig. 2.** (Color online) Snapshots of the density in the OM ( $n_1$ ) at  $t = 1200$ , for four turbulence simulations that differ only with respect to parallel resistivity ( $\eta = 1/\sigma_{12}$ ), magnetic field line fanning ( $f$ ) and shear ( $\xi$ ), i.e., “geometry” (G), as follows. (a):  $f = 1/4$  and  $\xi = 4$  (G: ON),  $\eta = 10^4$  ( $\eta$ : LOW). (b): G: ON,  $\eta = 10^5$  ( $\eta$ : HIGH). (c):  $f = 1$  and  $\xi = 0$  (G: OFF),  $\eta$ : LOW. (d):  $\eta$ : HIGH, G: OFF. Parameters common to all simulations are given in the text. High density is dark (red) at  $x \rightarrow 0$  and low density is dark again (blue) as  $x \rightarrow 50$ , on a white background representing the initial, quiescent SOL density.

**Fig. 3.** (Color online) A measure of the degree of electrical connection between the two regions based on the bloblet analysis: each point represents one blob recorded at  $x = 30$  in the OM.  $\Phi_1$  is measured at the center of the blob, and  $\Phi_2$  is measured at the magnetic field line image point in the XP. The identity line corresponds to perfect electrical connection. The simulations are labeled as in Figure 2 and color coded as in subsequent figures.

**Fig. 4.** (Color online) Character of the radial particle flux,  $\Gamma = nv_x$ , at  $x = 30$  in the OM: (a) time history of the poloidally-averaged flux  $\langle \Gamma \rangle_y$  and (b) probability distribution function  $P(\Gamma)$  versus  $\Gamma$ , normalized by the standard deviation  $\sigma_\Gamma$ . The four simulations are labeled as in Figure 2: (G:ON,  $\eta$ :LOW): dash-dotted (red); (G:ON,  $\eta$ :HIGH): solid gray (cyan); (G:OFF,  $\eta$ :LOW): dotted (magenta); (G:OFF,  $\eta$ :HIGH): solid black (blue).

**Fig. 5.** (Color online) (a) Poloidally and temporally averaged density,  $n(x)$ , (b) (negative) logarithmic derivative of  $n(x)$  and (c) skewness of density fluctuations,  $S(x)$ , as functions of radial location in the OM. The four simulations are labeled as in Figure 4.

**Fig. 6.** (Color online) Blob distribution in the OM at  $x = 30$ : (a) The *average* radial velocity (normalized by  $v_*$ ), versus half-width (normalized by  $a_*$ ), of all blobs having that half-width and for which the particle transport rate is positive ( $n_1 \cdot v_x \cdot a > 0$ ), and (b) the radial velocity versus half-width for *all* blobs, at that half-width, *filtered* by requiring that each represent a local maximum of density *with respect to x*. The curves  $(a/a_*)^{-2}$  and  $(a/a_*)^{1/2}$  reference the blob dispersion relation. (See Sec. III.) Different symbols represent the four simulations, as in Figure 2: (G:ON,  $\eta$ :LOW): filled diamonds (red); (G:ON,  $\eta$ :HIGH): open diamonds (cyan); (G:OFF,  $\eta$ :LOW): open boxes (magenta); (G:OFF,  $\eta$ :HIGH): filled boxes (blue).

## References

- <sup>1</sup> J. R. Myra, D. A. Russell and D. A. D'Ippolito, Phys. Plasmas **13**, 112502 (2006).
- <sup>2</sup> See for example T. C. Hender, B. A. Carreras, W. A. Cooper, J. A. Holmes, P. H. Diamond, and P. L. Similon, Phys. Fluids **27**, 1439 (1984), and references therein.
- <sup>3</sup> J. R. Myra, D. A. D'Ippolito, X. Q. Xu and R. H. Cohen, Phys. Plasmas **7**, 2290 (2000); Phys. Plasmas **7**, 4622 (2000).
- <sup>4</sup> B. Scott, Plasma Phys. Control. Fusion **39**, 1635 (1997).
- <sup>5</sup> B. N. Rogers, J. F. Drake, and A. Zeiler, Phys. Rev. Lett. **81**, 4396 (1998); B. N. Rogers and J. F. Drake, Phys. Rev. Lett. **79**, 229 (1997).
- <sup>6</sup> X. Q. Xu, W. M. Nevins, T. D. Rognlien, *et al.*, Phys. Plasmas **10**, 1773 (2003).
- <sup>7</sup> B. LaBombard, J. W. Hughes, D. Mossessian, M. Greenwald, B. Lipshultz, J. L. Terry, *et al.*, Nucl. Fusion **45**, 1658 (2005).
- <sup>8</sup> D. A. Russell, D. A. D'Ippolito, J. R. Myra, W. M. Nevins, and X. Q. Xu, Phys. Rev. Lett. **93**, 265001 (2004).
- <sup>9</sup> J.R. Myra and D. A. D'Ippolito, Phys. Plasmas **12**, 092511 (2005).
- <sup>10</sup> D. A. D'Ippolito and J. R. Myra, Phys. Plasmas **13**, 062503 (2006).
- <sup>11</sup> A. V. Nedospasov, Fiz. Plazmy **15**, 1139 (1989); [Sov. J. Plasma Phys. **15**, 659 (1989)].
- <sup>12</sup> D. Farina, R. Pozzoli, D. D. Ryutov, Nucl. Fusion **33**, 1315 (1993).
- <sup>13</sup> J. W. Connor and J. B. Taylor, Phys. Fluids **27**, 2676 (1984).
- <sup>14</sup> G. Q. Yu and S. I. Krasheninnikov, Phys. Plasmas **10**, 4413 (2003).
- <sup>15</sup> S. I. Krasheninnikov, Phys. Lett. A, **283**, 368 (2001); D. A. D'Ippolito, J. R. Myra, and S. I. Krasheninnikov, Phys. Plasmas **9**, 222 (2002).
- <sup>16</sup> S.J. Zweben, R.J. Maqueda, D.P. Stotler, A. Keese, J. Boedo, et al., Nucl. Fusion **44** 134 (2004); O. Grulke, J. L. Terry, B. LaBombard and S. J. Zweben, Phys. Plasmas **13**, 012306 (2006).
- <sup>17</sup> A. Y. Aydemir, Phys. Plasmas **12**, 062503 (2005).
- <sup>18</sup> J. R. Myra, J. Boedo, B. Coppi, D. A. D'Ippolito, S. I. Krasheninnikov, et al., in *Plasma Physics and Controlled Nuclear Fusion Research 2006* (IAEA, Vienna, 2007), paper IAEA-CN-149-TH/P6-21.
- <sup>19</sup> The growth rate is found by solving the dispersion relation, Eq. (8) in Paper I, extended to include the dissipative terms in the present simulations and evaluating  $v(x)$  and  $\gamma_{\text{mhd}}^2 = -\beta (k_{y1}^2 / k_{\perp 1}^2) \partial_x \ln n_0(x)$  at that  $x$  for which the (-)logarithmic derivative of  $n_0$  is maximized. The *initial* conditions are all in the RB regime, and therefore the growth rates are independent of fanning and shear.
- <sup>20</sup> G. Q. Yu and S. I. Krasheninnikov, Phys. Plasmas **10**, 4413 (2003).
- <sup>21</sup> J.R. Myra and D. A. D'Ippolito, Phys. Plasmas **12**, 092511 (2005).

- <sup>22</sup> M. N. Rosenbluth and C. L. Longmire, *Ann. Phys.* **1**, 120 (1957).
- <sup>23</sup> G. Y. Antar, S. I. Krasheninnikov, P. Devynck, R. P. Doerner, E. M. Hollmann, J. A. Boedo, S. C. Luckhardt and R. W. Conn, *Phys. Rev. Lett.* **87**, 065001 (2001).
- <sup>24</sup> G. Y. Antar, B. Counsell, Y. Yu, B. LaBombard, and P. Devynck, *Phys. Plasma* **10**, 419 (2003).
- <sup>25</sup> J. A. Boedo, D. Rudakov, R. Moyer, S. Krasheninnikov, D. Whyte, et al. *Phys. Plasmas* **8**, 4826 (2001).
- <sup>26</sup> D. Rudakov, J. A. Boedo, R. Moyer, S. Krasheninnikov, A. W. Leonard, et al., *Plasma Phys. Control. Fusion* **44**, 717 (2002).
- <sup>27</sup> S. I. Krasheninnikov, A. Yu. Pigarov, S.A. Galkin, et al., in *Proceedings of the 19th IAEA Fusion Energy Conference*, Lyon, France, 2002 (IAEA, Vienna, 2003), paper IAEA-CN-94/TH/4-1.
- <sup>28</sup> J.L. Terry, N.P. Basse, I. Cziegler, M. Greenwald, O. Grulke, B. LaBombard, S.J. Zweben, et al., *Nucl. Fusion* **45**, 1321 (2005).
- <sup>29</sup> J. R. Myra, D. A. D'Ippolito, D. P. Stotler, S. J. Zweben, B. P. LeBlanc, J.E. Menard, R. J. Maqueda, and J. Boedo, *Phys. Plasmas* **13**, 092509 (2006).
- <sup>30</sup> J. A. Boedo, D. L. Rudakov, R. A. Moyer, G. R. McKee, R. J. Colchin, et al., *Phys. Plasmas* **10**, 1670 (2003).
- <sup>31</sup> I. Furno, B. Labit, M. Podesta, A. Fasoli, et al., private communication [2007], (to be submitted to PRL).
- <sup>32</sup> See the BOUT code results in Fig. 11 of Ref. [30], for example.
- <sup>33</sup> M. Spolaore, V. Antoni, E. Spada, H. Bergsaker, R. Cavazzana, J. R. Drake, E. Martines, G. Regnoli, G. Serianni, and N. Vianello, **93**, 215003 (2004).
- <sup>34</sup> M. Agostini, S. Zweben, R. Cavazzana, P. Scarin, G. Serianni, R. J. Maqueda, and D.P. Stotler, private communication [2007], (to be submitted to *Phys. Plasmas*).
- <sup>35</sup> J. A. Boedo, D. Rudakov, R. Moyer, S. Krasheninnikov, D. Whyte, et al. *Phys. Plasmas* **8**, 4826 (2001).
- <sup>36</sup> O. Garcia, V. Naulin, A. H. Nielsen, and J. Juul Rasmussen, *Phys. Plasmas* **12**, 062309 (2005).
- <sup>37</sup> The normalization of  $\langle n \rangle$  in  $f_p = \langle n \rangle / n_b$  is the total number of blobs, i.e.,  $\langle n \rangle = \sum_i n_i / N$ , where  $\sum_i$  is restricted to the filtered subset of blobs, and  $N$  is the total number of blobs in the unfiltered universe.
- <sup>38</sup> V. Naulin, private communication [2007].
- <sup>39</sup> M.V. Umansky, , T.D. Rognlien and X.Q. Xu, *J. Nucl. Mater.* **337-339**, 266 (2005).
- <sup>40</sup> R.H. Cohen and D. D. Ryutov, *Nucl. Fusion* **37**, 621 (1997); D. D. Ryutov and R. H. Cohen, *Contrib. Plasma Phys.* **44**, 168 (2004).
- <sup>41</sup> S. T. Zalesak, *J. Comp. Phys.* **31**, 335 (1979), and references therein.
- <sup>42</sup> W. H. Press, S. A. Teukolsky, W. T. Vetterling and B. P. Flannery, *Numerical Recipes in Fortran 77: The Art of Scientific Computing*, 2<sup>nd</sup> ed., p840 (1996).

<sup>43</sup> P. N. Swarztrauber, *SIAM Review* **19**(3), 490 (1977).

<sup>44</sup> M. Farge, *Annu. Rev. Fluid Mech.* **24**, 395 (1992).

Figure 1

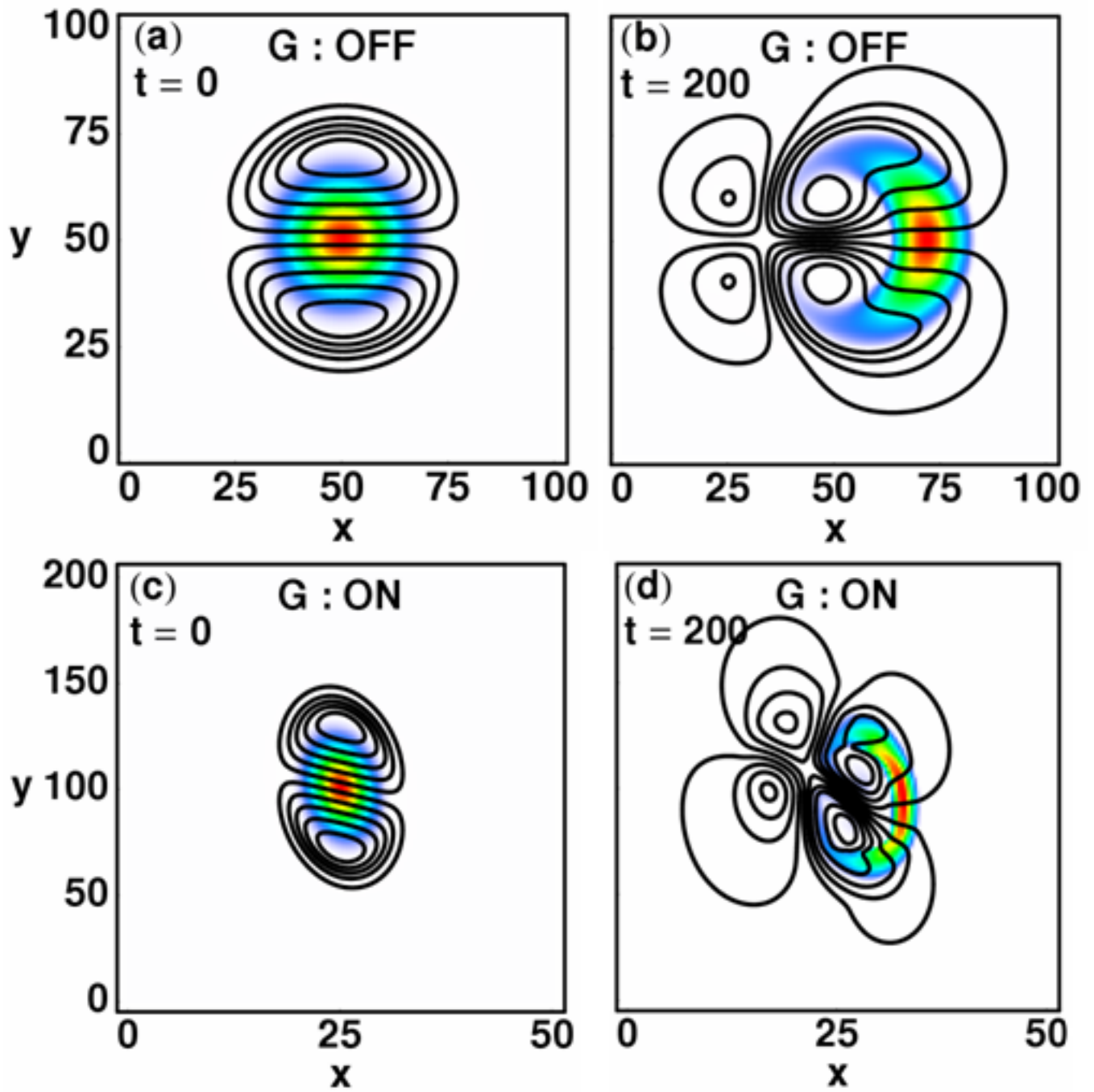


Figure 2

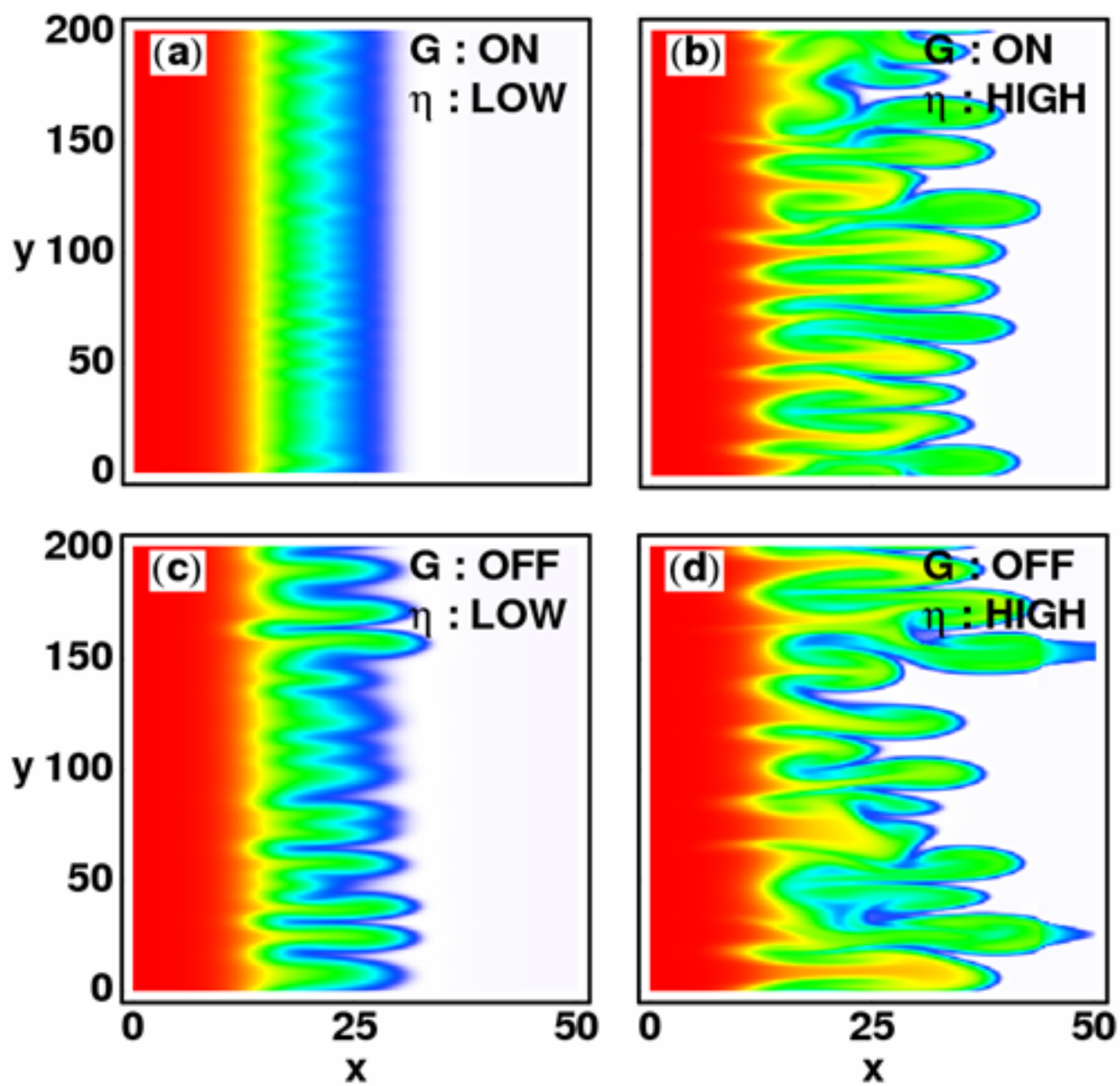


Figure 3

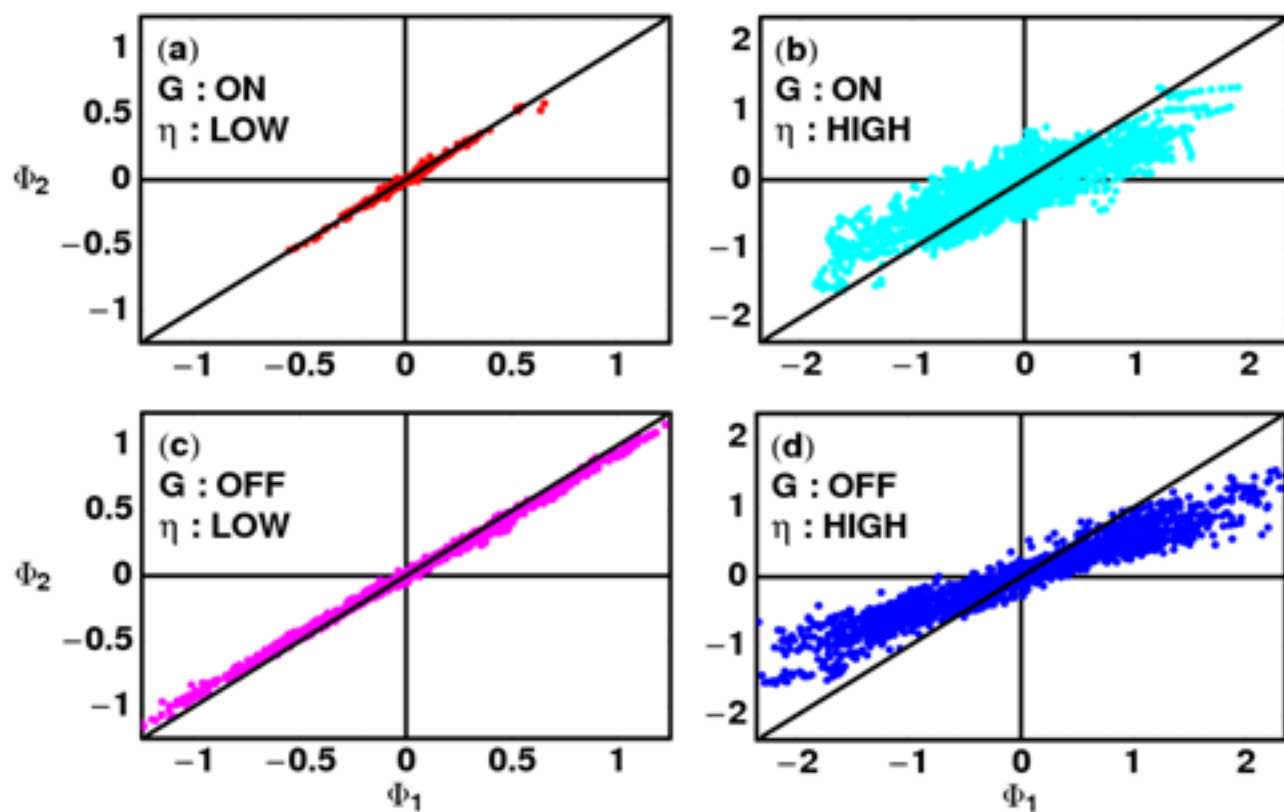


Figure 4

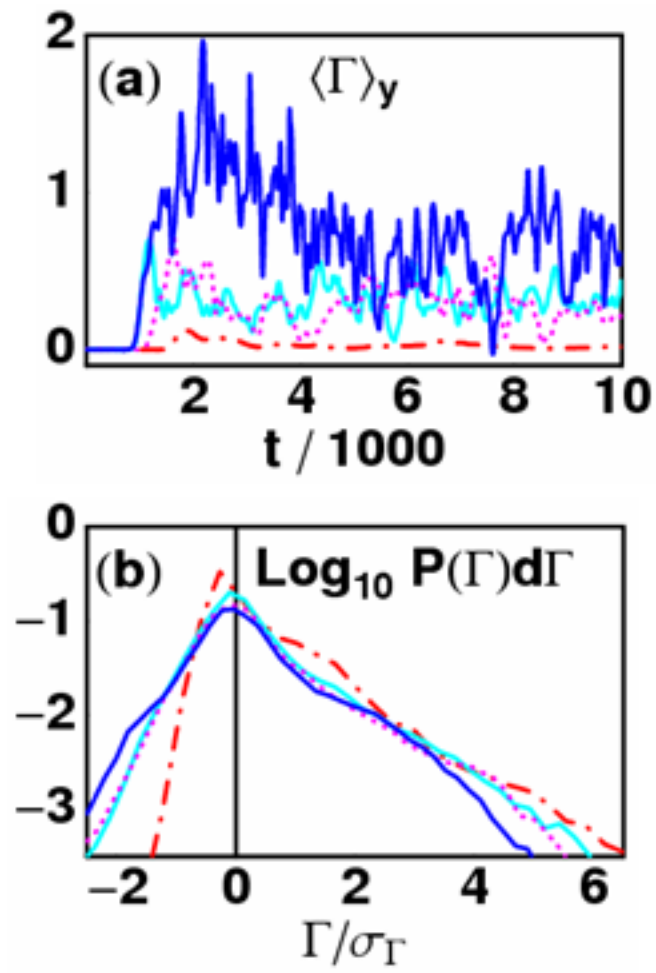


Figure 5

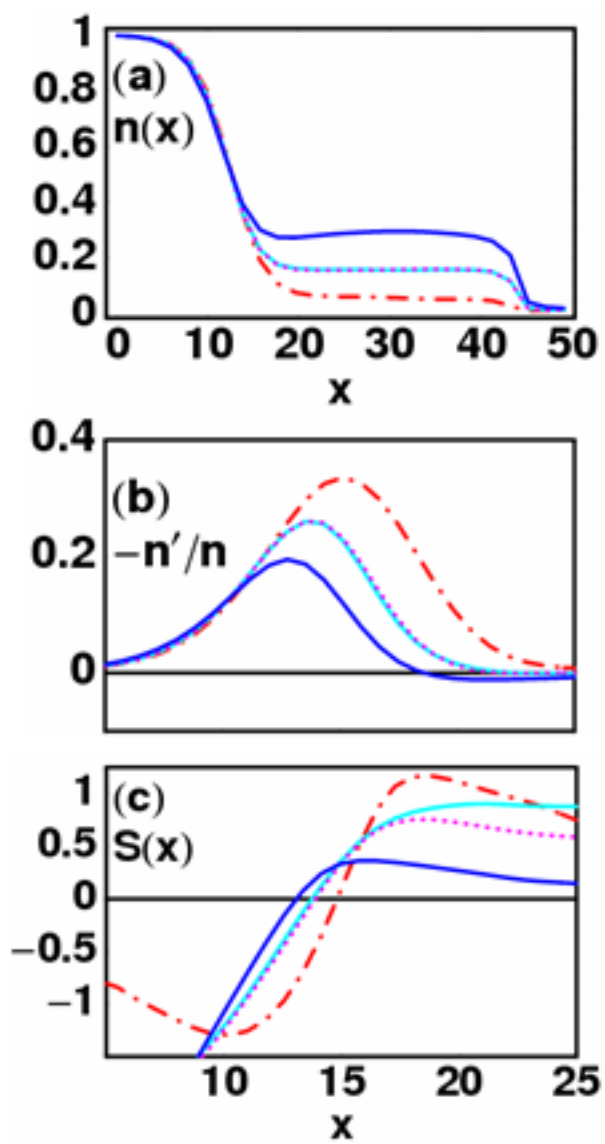


Figure 6

